Numerically derived parametrisation of optimal RMP coil phase as a guide to experiments on ASDEX Upgrade

D A Ryan[1 2], Y Q Liu[2], L Li[3], A Kirk[2], M Dunne[4], B Dudson[1], P Piovesan[5], W Suttrop[4], M Willensdorfer[4], the ASDEX Upgrade team[4] and the EUROfusion MST1 team [1]

[1] York Plasma Institute, Department of Physics, University of York, York,YO10 5DQ, UK

[2] CCFE, Culham Science Centre, Abingdon, Oxfordshire, OX14 3DB, UK

[3] College of Science, Donghua University, Shanghai 201620, China

[4] Max Planck Institute for Plasma Physics, Garching, Germany

[5] Consorzio RFX, Corso Stati Uniti, 4, 35127, Padova, Italy

Abstract.

Edge Localised Modes (ELMs) are a repetitive MHD instability, which may be mitigated or suppressed by the application of resonant magnetic perturbations (RMPs). In tokamaks which have an upper and lower set of RMP coils, the applied spectrum of the RMPs can be tuned for optimal ELM control, by introducing a toroidal phase difference $\Delta\Phi$ between the upper and lower rows. The magnitude of the outermost resonant component of the RMP field $|b^1_{res}|$ (other proposed criteria are discussed herein) has been shown experimentally to correlate with mitigated ELM frequency, and to be controllable by $\Delta\Phi$ (Kirk *et al* 2013 *Plas. Phys. Cont. Fus.* **53** 043007). This suggests that ELM mitigation may be optimised by choosing $\Delta\Phi = \Delta\Phi_{opt}$, such that $|b^1_{res}|$ is maximised. However it is currently impractical to compute $\Delta\Phi_{opt}$ in advance of experiments. This motivates this computational study of the dependence of the optimal coil phase difference $\Delta\Phi_{opt}$, on global plasma parameters β_N and q_{95}, in order to produce a simple parametrisation of $\Delta\Phi_{opt}$. In this work, a set of tokamak equilibria spanning a wide range of (β_N, q_{95}) is produced, based on a reference equilibrium from an ASDEX Upgrade experiment. The MARS-F code (Liu *et al* 2000 *Phys. Plasmas* **7** 3681) is then used to compute $\Delta\Phi_{opt}$ across this equilibrium set for toroidal mode numbers $n = 1 - 4$, both for the vacuum field and including the plasma response. The computational scan finds that for fixed plasma boundary shape, rotation profiles and toroidal mode number n, $\Delta\Phi_{opt}$ is a smoothly varying function of (β_N, q_{95}). A 2D quadratic function in (β_N, q_{95}) is used to parametrise $\Delta\Phi_{opt}$, such that for given (β_N, q_{95}) and n, an estimate of $\Delta\Phi_{opt}$ may be made without requiring a plasma response computation. To quantify the uncertainty of the parametrisation relative to a plasma response computation, $\Delta\Phi_{opt}$ is also computed using MARS-F for a set of benchmarking points. Each benchmarking point consists of a distinct free boundary equilibrium reconstructed from an ASDEX Upgrade RMP experiment, and set of experimental kinetic profiles and coil currents. Comparing the MARS-F predictions of $\Delta\Phi_{opt}$ for these benchmarking points to predictions of the 2D quadratic, shows that relative to a plasma response computation with MARS-F the 2D quadratic is accurate to 26.5 degrees for $n = 1$, and 20.6 degrees for $n = 2$. Potential sources for uncertainty are assessed.

1. Introduction

Edge Localised Modes (ELMs) are a repetitive MHD instability, driven by the high current densities and pressure gradients found at the edge of high confinement mode tokamak plasmas [2, 3]. Extrapolation from current machines suggests that, if left unmitigated, ELMs pose a hazard to the plasma facing components of the ITER tokamak [4].

It has been shown that ELMs can be mitigated - an increase in the ELM frequency, accompanied by a decrease in individual ELM size - by the application of Resonant Magnetic Perturbations (RMPs) using dedicated magnetic coils, and ELM mitigation by RMPs has now been demonstrated on most medium and large sized tokamaks [1, 5–9]. Presently, most tokamaks have two sets of RMP coils, one toroidal ring of 6-12 coils above the midplane, and another below. The currents in the discrete coil sets are typically chosen to have an approximately sinusoidal dependence in the toroidal direction, with a single dominant toroidal mode number n. Having two sets of coils allows the poloidal spectrum to be tuned by introducing a toroidal phase offset between the upper and lower coil currents, defined here as $\Delta\Phi = \Phi_{upper} - \Phi_{lower}$, where Φ_{upper} and Φ_{lower} are the phases of the dominant n component of the upper and lower toroidal current waveforms respectively. $\Delta\Phi$ may be varied independently of the global plasma parameters, so for a given set of plasma parameters it may be used to optimise the applied field by choosing a value $\Delta\Phi_{opt}$, which maximises some figure of merit. Numerous figures of merit have been proposed as discussed below, all of which require a computation of the plasma response to quantify, which complicates prediction of $\Delta\Phi_{opt}$ ahead of experiments. The aim of this work is to create an accessible map of $\Delta\Phi_{opt}$ with quantified uncertainty, which researchers may use to optimise experimental RMP fields without requiring a plasma response computation.

It is well known that to correctly interpret magnetic perturbation experiments, it is necessary to include the plasma response to the applied perturbation [10–16]. A review of approaches to computing the plasma response to applied perturbations can be found in [17]. The plasma response calculations in this work are performed using MARS-F [18], which numerically solves the linearised equations of resistive MHD including toroidal geometry and toroidal rotation, using realistic experimental tokamak equilibria and applied coil currents. MARS-F has been well validated against experiments on DIII-D and benchmarked against other codes [19–21]. The perturbation is approximated as having a single n sinusoidal dependence in the toroidal direction, we therefore ignore the effects of toroidal sidebands which are expected to be small compared to the dominant n component [22].

By searching for correlations between aspects of the plasma response to the applied RMPs and experimentally observed effects of the RMPs, several candidate figures of merit for predicting RMP effects on ELMs have been proposed. The resonant component $|b^1_{res}|$ (also b^r_{res} in some works, which differs only in normalisation) is the amplitude of the component of the magnetic perturbation aligned to the equilibrium magnetic field (satisfying $m = nq$) closest to the plasma edge. Correlations have been detected between $|b^1_{res}|$ and

mitigated ELM frequency on ASDEX Upgrade and MAST [23, 24]. As well as the magnetic perturbation, the applied RMP also induces a displacement of the plasma which may be predicted numerically and measured experimentally [25, 26]. ξ_X refers to the maximum RMP induced displacement of the plasma boundary in the region of the X-point, and has been shown to correlate with density pump out on MAST [27, 28], and with mitigated ELM frequency on ASDEX Upgrade [23]. The high field side (HFS) response refers to the magnitude of the magnetic perturbation at the high field side midplane. The HFS response, both measured experimentally and predicted numerically, has been shown to correlate with density pump out and ELM suppression on DIII-D [16, 29]. The edge peeling response refers to amplification of marginally stable MHD modes [30], localised near the plasma edge and with poloidal harmonic numbers above resonance ($m > nq$). Correlations have been detected between the edge peeling response and ELM suppression on DIII-D [15, 22], density pump out on MAST [27], and ELM mitigation on ASDEX Upgrade [23, 31].

These diverse observed correlations are shown to be self consistent by modelling works, which explain that as functions of $\Delta\Phi$ these figures of merit are strongly correlated with each other. It was shown previously that the displacement component of the amplified peeling response is responsable for driving ξ_X [27], and the also that the magnetic component of the peeling response can drive $|b^1_{res}|$ via poloidal harmonic coupling [22, 31, 32], a mechanism previously proposed to interpret error field correction experiments on NSTX and DIII-D [14]. Furthermore, examining the linearised equations of ideal MHD provides a direct relation between ξ_X and b^1_{res} [33], explaining why these three are often seen to be strongly correlated in modelling works [23, 34, 35]. Meanwhile, it is also shown computationally that the HFS response also shares the same $\Delta\Phi$ dependence as ξ_X and $|b^1_{res}|$ [16, 29]. Therefore in the context of optimising over $\Delta\Phi$, the figures of merit $|b^1_{res}|$, ξ_X, the peeling response and the HFS response are all equivalent. Of these four, this work chooses to use $|b^1_{res}|$ for ease of computation, but the results will apply to any of the figures of merit discussed above. Thus $\Delta\Phi_{opt}$ is defined here as $\Delta\Phi$ for which $|b^1_{res}|$ is maximised.

It must also be noted that in a recent work, it is shown that the amplified peeling response can cause ELMs to reappear in ELM suppressed discharges on DIII-D, by pushing the equilibrium closer to the peeling-ballooning stability limit and thereby increasing the probability of ELMs [36]. This complicates the picture in the context of ELM suppression, but in the context of ELM mitigation it supports the premise that the amplified peeling response may drive ELMs prematurely unstable and hence increase the mitigated ELM frequency. Furthermore, DIII-D experiments [37, 38] suggest that ELM suppression may be triggered by the co-location of a rational surface of the RMP, the pedestal top and the $\omega_{\perp e} = 0$ location (where the electron perpendicular flow vanishes), which we here call the 'co-location' criterion. However this criterion is not expected to be controllable by the coil phasing $\Delta\Phi$, and so is not considered in this work. Implications of these two results for RMP optimisation for ELM suppression are also not considered in this work, which instead focusses on optimising RMP fields for ELM mitigation.

It is well demonstrated experimentally [5, 15, 28, 29, 39–42] and computationally [22, 29, 33, 34, 43, 44] that RMP induced ELM effects are sensitive to the plasma safety factor at the 95% poloidal magnetic flux surface q_{95}. In particular, recent computational scaling studies [22, 34] show that $\Delta\Phi_{opt}$ varies approximately linearly with q_{95}. Observed ELM effects and computed $\Delta\Phi_{opt}$ are also known to be sensitive to the plasma shape [34, 39], but this dependence is not studied here. In this work, the dependence of $\Delta\Phi_{opt}$ on the normalised beta β_N and q_{95}, is numerically investigated and quantified for ASDEX Upgrade plasmas. Normalised beta β_N is defined as $\beta_N = \beta(\%)a(m)B_0(T)/I_p(MA)$, where a is the plasma minor radius, B_0 is the equilibrium magnetic field at the magnetic axis, I_p is the total plasma current, and β is the normalised plasma pressure $\beta = 2\mu_0 <p>/<B^2>$, where $<..>$ denotes an average over the plasma volume. A reference plasma equilibrium from the ASDEX Upgrade tokamak is scaled in pressure and current, to create a set of equilibria spanning a wide parameter space in (β_N, q_{95}), which covers the parameters most typically accessed in ASDEX Upgrade experiments. At each point in (β_N, q_{95}) space and for toroidal mode numbers $n = 1 - 4$, the plasma response to an applied perturbation is computed by solving the linearised equations of resistive MHD in full toroidal geometry using the code MARS-F [18], and the optimal coil phasing $\Delta\Phi_{opt}$ computed. It is found that $\Delta\Phi_{opt}$ increases smoothly with q_{95}, consistent with previous computational scans [22, 29, 34]. However a previous experimental and computational study found $\Delta\Phi_{opt}$ to be insensitive to β_N [29], in contrast to this work which finds a weak decrease in $\Delta\Phi_{opt}$ with β_N. A simple 2D quadratic function is proposed to parametrize the dependence of $\Delta\Phi_{opt}$ on (β_N, q_{95}). The coefficients of this function are computed by linear regression, and included here for researchers to use as a guide for future RMP experiments on ASDEX Upgrade. To evaluate the utility of the 2D quadratic function for predicting $\Delta\Phi_{opt}$ (relative to a prediction using a MARS-F plasma response computation), the plasma response to applied perturbations is computed for a set of equilibria and kinetic profiles which are taken directly from a large set of distinct ASDEX Upgrade experiments, with significant variation in β_N and q_{95}, as well as plasma shape, rotation and kinetic profiles. For each of these benchmarking points, $\Delta\Phi_{opt}$ is computed, and by comparing the 2D quadratic to these benchmarking points, it is determined that the 2D quadratic is able to predict $\Delta\Phi_{opt}$ to within 26 degrees of a plasma response computation for $n = 1$ RMPs, and within 21 degrees for $n = 2$ RMPs, for most experimentally accessible (β_N, q_{95}) values. This parametrisation and error estimate are the primary results of this work. It should be noted that for $n = 4$, only odd and even phases ($\Delta\Phi$=180,0) are experimentally accessible with the ASDEX Upgrade coil set, so high accuracy is not required when predicting $\Delta\Phi_{opt}$. Due to limited available data, the benchmarking procedure for $n = 3, 4$ is left for future work. To investigate possible sources of uncertainty in the 2D quadratic, $\Delta\Phi_{opt}$ is computed for scans of the pedestal width and amplitude of toroidal rotation, which find that $\Delta\Phi_{opt}$ is robust to both. This suggests that neither of these factors contribute strongly to the computed uncertainty in $\Delta\Phi_{opt}$, and the plasma shape is suggested as the primary source of uncertainty.

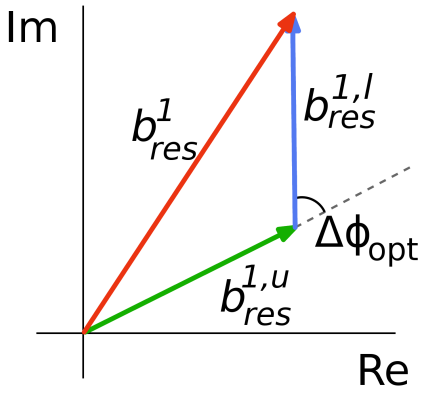

Figure 1. The pitch aligned component $|b^1_{res}|$ is maximised when $b^{1,u}_{res}$ and $b^{1,l}_{res}$ are parallel in the complex plane.

2. Alignment of applied field with equilibrium field

2.1. Extracting $\Delta\Phi_{opt}$ from a plasma response computation

In this work, the plasma response due to the upper and lower coils (b^u and b^l respectively) are computed separately, the field due to both coils are reconstructed in post process as $b^t = b^u + b^l e^{(-i\Delta\Phi)}$. This is valid because MARS-F is a linear code, so the sum of two solutions is also a solution. For a given outermost pitch aligned component due to upper coils $b^{1,u}_{res}$, and lower coils $b^{1,l}_{res}$ (both complex valued scalars), the total outermost pitch aligned component $|b^1_{res}| = |b^{1,u}_{res} + b^{1,l}_{res} e^{(-i\Delta\Phi)}|$ is maximised when $b^{1,u}_{res}$ and $b^{1,l}_{res}$ are parallel in the complex plane. Therefore the optimal coil phase is simply the angle between $b^{1,u}_{res}$ and $b^{1,l}_{res}$ in the complex plane, given by equation 1 below.

$$\Delta\Phi_{opt} = \pm arccos\left(\frac{b^{1,l}_{res} \cdot b^{1,u}_{res}}{|b^{1,l}_{res}||b^{1,u}_{res}|}\right) \tag{1}$$

This concept is described visually in figure 1. This formula eliminates the need for a numerical scan of $\Delta\Phi$ to determine $\Delta\Phi_{opt}$ as used in previous works [35]. To account for the sign uncertainty in Equation 1, it is necessary to determine the sign of $\Delta\Phi_{opt}$ by comparing $|b^{1,u}_{res} + b^{1,l}_{res} e^{(-i\Delta\Phi_{opt})}|$ and $|b^{1,u}_{res} + b^{1,l}_{res} e^{(+i\Delta\Phi_{opt})}|$, and choosing the larger. Figure 2 demonstrates that computing $\Delta\Phi_{opt}$ using Equation 1, yields the same result as a conventional $\Delta\Phi$ scan.

2.2. Effect on alignment of equilibrium parameters β_N and q_{95}

The parameters β_N, q_{95} and n are chosen for this dependence study, because the spectral alignment of the applied perturbation with the equilibrium field (ie, the extent to which the

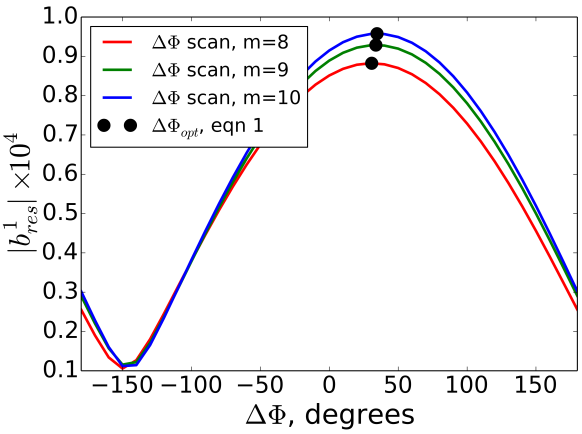

Figure 2. Previous works [32, 34, 35] have computed $\Delta\Phi_{opt}$ using a scan of $\Delta\Phi$, which is time consuming and limits the precision of $\Delta\Phi_{opt}$ to the scan step size. In this figure, $\Delta\Phi_{opt}$ computed using Equation 1 is compared with a $\Delta\Phi$ scan of $|b^1_{res}|$. It shows that the Equation 1 yields the same value for $\Delta\Phi_{opt}$ as a scan of $\Delta\Phi$.

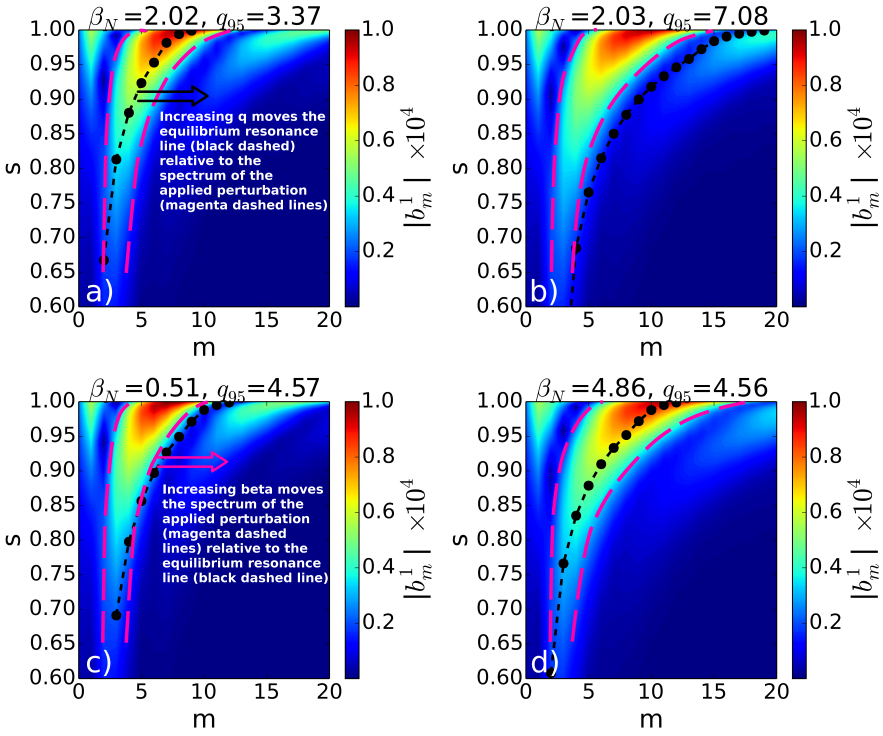

Figure 3. a) and b) shows the $nq(s) = m$ line relative to the vacuum spectrum for a low (a) and high (b) q_{95} case, with identical β_N. This demonstrates how changing q_{95} or n moves the $nq(s) = m$ line relative to the spectrum of the applied perturbation. c) and d) shows the $nq(s) = m$ line relative to the vacuum spectrum for a low (a) and high (b) β_N case, with identical q_{95}. Increasing plasma pressure β_N moves the magnetic axis outwards, which distorts the equilibrium magnetic geometry on the outboard side, such that the vacuum spectrum is shifted to higher m.

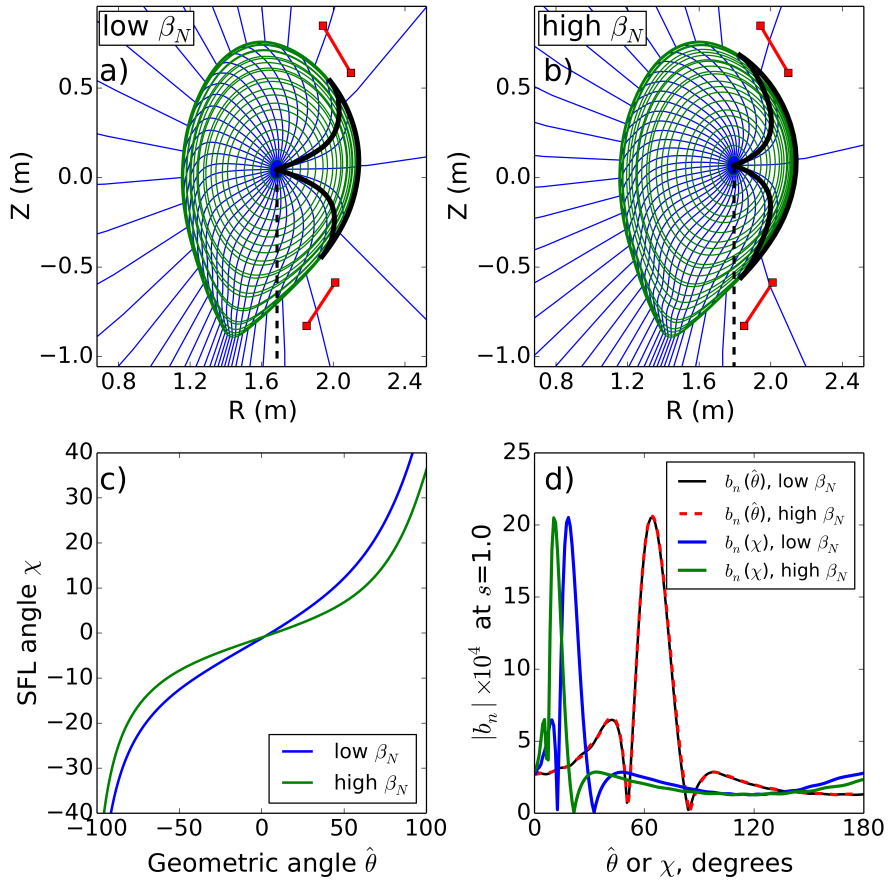

Figure 4. a,b) Grids showing the equilibrium based straight field line coordinate systems for low (0.51) and high (4.86) β_N cases. Note these are extreme examples of high and low β_N, chosen to best illustrate the effect. On both grids, the black solid bold lines are lines of $\chi = \pm 15$. The high β_N case shows Shrafanov shift of the magnetic axis, and also that $\chi = \pm 15$ encompasses a larger arclength of the plasma boundary. c) The generalised poloidal angle χ against geometric angle $\hat{\theta}$. The high β_N case shows a lower $d\chi/d\theta$ on the high field side, so the same geometric features are represented with a smaller extent of χ. d) The normal component of the applied vacuum perturbation at the plasma boundary for a high and low β_N case, plotted against geometric coordinate $\hat{\theta}$ to show that in real space both applied fields are the same, and plotted against generalised poloidal angle χ to show how the high and low β_N fields differ when represented in SFL coordinates, due to the redistribution of χ with changing β_N. Notice that in the high β_N case, the main peaks of the applied field (which naturally occur near the RMP coils) are compressed into a narrower range of χ, causing the poloidal spectrum to be shifted towards higher m.

applied perturbation aligns with the $m = nq$ line in (m,s) space, where $s = \psi_N^{1/2}$ is the radial coordinate and m is the poloidal harmonic number), is expected to be modified by these parameters, and they therefore affect the optimal coil phasing $\Delta\Phi_{opt}$. Figure 3 shows the effect on the applied vacuum spectrum and equilibrium resonance line (satisfying $m = nq$), of changing q_{95} and plasma β_N. Figure 3a) and b) show that for constant β_N, increasing q_{95} or n moves the $m = nq$ line in (m, s) space to higher m, thereby moving the resonant component relative to the applied spectrum. Figure 3c) and d) show that for constant q_{95}, changing β_N

distorts the spectrum of the applied field relative to the $m = nq$ line, modifying alignment as explained in more detail below. This result justifies the choice of q_{95} and β_N as independent variables for this study.

The dependence of field alignment on β_N is explained in Figure 4. Physically relevant poloidal harmonics may only be rigorously defined in a straight field line (SFL) coordinate system, in which the poloidal angle is not the geometric poloidal angle θ, but the generalised poloidal angle χ, which is defined such that field lines are straight in the (χ,ϕ) plane where ϕ is the toroidal angle. χ and m are therefore defined relative to the magnetic equilibrium. Figure 4a,b) shows the SFL based grid for a high and low β_N case. In the high β_N case the magnetic axis is shifted outwards by shrafranov shift (shown by the vertical dashed lines). Solid black lines in the figure are lines of $\chi = \pm 15$ degrees and the plasma boundary enclosed by this angular range. It shows that in the high β_N case, on the high field side where the RMPs are applied, a given range of χ encloses a much larger arclength of the plasma boundary than the low β_N case. The RMP coils and applied field are identical in both cases in real (R, Z) space, but the field in SFL coordinates changes with β_N, because the definition of the SFL poloidal angle χ, relative to geometric angle θ, changes with β_N. Figure 4c) shows the generalised poloidal angle χ against geometric angle $\hat{\theta}$ (where $\hat{\theta}$ is measured from an origin common to both the high and low β_N cases, rather than the magnetic axis). The figure shows that increasing β_N causes a redistribution of χ relative to $\hat{\theta}$. Figure 4d) shows the effect this has on the vacuum magnetic perturbation at the plasma boundary as a function of χ. The figure shows that in geometric coordinates the fields are the same, as expected, but SFL coordinates they differ. In particular, in the high β_N case, the main features of the perturbation (closest to the coils) are compressed into a smaller range of χ, which means they are represented with higher poloidal mode numbers. This is the cause of the spectral shift towards higher m with increasing β_N apparent in figure 3c,d).

It is acknowledged here that the plasma boundary shape, via its influence on the equilibrium geometry near the edge, should also have a significant impact on alignment. This is not included in this work, since the plasma boundary shape is not described by a single scalar value, and so would add too many extra dimensions to consider here. The dependence of $\Delta\Phi_{opt}$ on the plasma boundary shape is investigated partially in [34].

3. Dependence of $\Delta\Phi_{opt}$ with q_{95}, β_N, n

3.1. Scaled equilibrium set

Using the CHEASE fixed boundary equilibrium solver [45], a dense set of equilibria which span a wide range of β_N and q_{95} were produced by scaling a reference equilibrium from ASDEX Upgrade experiment 30835 at 3.2s, which is used as a standard equilibrium in many modelling works [32, 35]. The reference equilibrium was first truncated to exclude the X

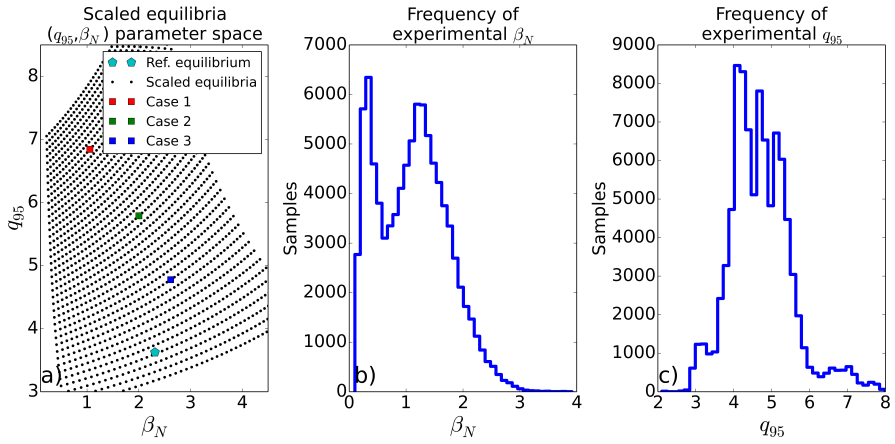

Figure 5. a) The set of equilibria (black dots) were made by scaling the reference equilibrium (cyan pentagon) in plasma pressure and plasma current. The coloured squares correspond to the 3 example cases plotted in Figure 6. b) Histogram of experimental β_N values and c) Histogram of experimental q_{95} values. Values are gathered from 20 timepoints from the flattops of 4600 recent ASDEX Upgrade plasma discharges. Note also that q_{95} is defined as always positive in this work.

point, by manually smoothing the plasma boundary in the vicinity of the X point. The resulting boundary shape was held constant in this scan. q_{95} was scanned by scanning the forced value of the core safety factor q_0, resulting in a rigid shift of the q profile (including edge safety factor q_a) and self-consistent adjustments to the current and pressure profiles. To scan β_N the pressure was scaled self similarly, with self-consistent adjustments to the current and q profiles, with the constraint that q_0 be fixed. The inductance l_i was also constant to within 5%. Figure 5a) shows the (β_N, q_{95}) values of the scaled equilibrium set produced, the reference equilibrium, and three example cases for which profiles are plotted in figure 6. Each dot represents an individual equilibrium point. Figure 5b,c) shows histograms of experimentally accessed values of q_{95} and β_N, taken from 20 timepoints from the flattops of 4600 ASDEX Upgrade plasma discharges. The figure shows that the equilibrium set is wide enough in β_N and q_{95} to encompass the most commonly accessed ASDEX Upgrade global plasma parameters. Figure 6 shows the q, pressure and current profiles for 3 of the scaled equilibria as annotated in Figure 5a), to demonstrate the rigid shift of the q profile, and the scaling of the pressure and current profiles.

3.2. $\Delta\Phi_{opt}$ computed using MARS-F across (β_N, q_{95}) domain

For each point in the (β_N, q_{95}) scaled set and for $n = 1 - 4$, the vacuum field and plasma response to the applied RMP field were computed, by solving the linearised equations of resistive MHD using the MARS-F code. The field due to the upper and lower coils were computed separately, to compute the outermost resonant field component due to the upper coil set $b^{1,u}_{res}$, and lower coil set $b^{1,l}_{res}$. The optimal coil phase was then computed using Equation 1.

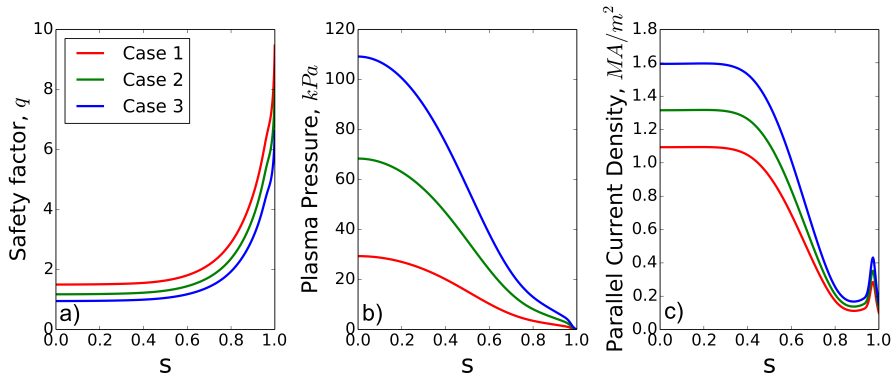

Figure 6. a) q_{95} was scanned by changing the forced value of q_0, resulting in a rigid shift of the q profile b) β_N was scaled by scaling the pressure profile c) The current density varies consistent with the plasma pressure and safety factor, which are the two variables used to scale q_{95} and β_N. Case 1,2,3 are used to refer to the coloured points in Figure 5a).

Figure 7 shows $\Delta\Phi_{opt}$ for the scan of (β_N, q_{95}), for $n = 1 - 4$, in the vacuum approximation and including the plasma response. In figure 7, the range of $\Delta\Phi_{opt}$ can exceed 360 degrees. This is because phase wraps were manually removed in this study, since they do not represent physics and obscure the underlying trends. Generally, $\Delta\Phi_{opt}$ increases with q_{95}, and decreases with β_N. As found previously [22, 34, 35], the strongest dependence is on q_{95}.

This work also finds a weak β_N dependence of $\Delta\Phi_{opt}$, in contrast with a previous work [29] in which a similar β_N scan was performed both experimentally and numerically and found that β_N has no effect on $\Delta\Phi_{opt}$. In [29], β_N is scaled by modifying the core pressure profile while leaving the pressure pedestal approximately unchanged, whereas in this work β_N is modified by scaling the entire pressure profile including the pedestal by a constant factor as shown in Figure 6b). $|b^1_{res}|$ is defined at the last rational surface, which is typically very close to the plasma edge near the pedestal foot. It is possible that in the former approach in which pressure pedestal is approximately unchanged in the β_N scan, the equilibrium in the edge region is relatively unchanged by β_N scaling. Therefore the alignment of the perturbation with the equilibrium field in the pedestal would not be changed by β_N, explaining the absence of a β_N dependence of $\Delta\Phi_{opt}$. Conversely if β_N is scaled by multiplying pressure profile by a constant factor, as in this work, the pressure pedestal scales with β_N, and therefore we would expect a change in alignment with β_N as explained in Figure 3. This may explain why the numerical approach in [29] does not detect a change in $\Delta\Phi_{opt}$ with β_N, whereas the approach in this work does. This suggests that whether or not a β_N dependence is detected depends on whether the pedestal pressure is allowed to scale with β_N. However, the result in [29] is also supported by experimental measurements which detect no $\Delta\Phi_{opt}$ dependence on β_N, suggesting that the β_N scaling approach adopted in [29] corresponds closer to the physical reality. Investigating whether the β_N dependence can be detected in ASDEX Upgrade experiments is left to future work.

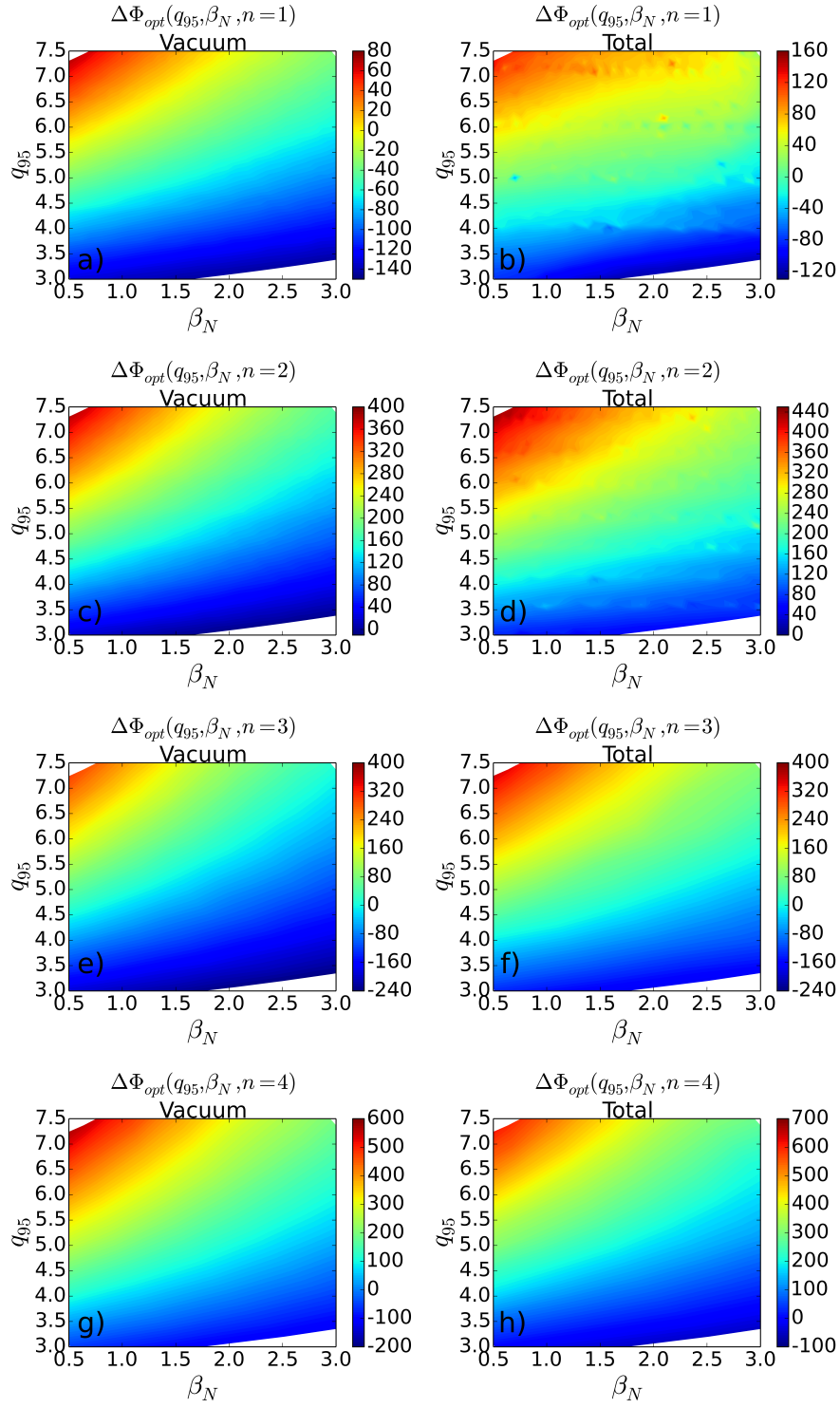

Figure 7. $\Delta\Phi_{opt}$ computed at each point of the scaled equilibium set using MARS-F to compute $b^{1,u}_{res}$ and $b^{1,l}_{res}$, and Equation 1 for $\Delta\Phi_{opt}$. a,c,e,g) Optimal alignment of the vacuum field for $n = 1, 2, 3, 4$ respectively. b,d,f,h) Optimal alignment of the total field for $n = 1, 2, 3, 4$ respectively. In all cases $\Delta\Phi_{opt}$ varies smoothly with β_N and q_{95}.

$RMSE_{poly}$	Linear	Quadratic	Cubic
n=1 vacuum	6.65	0.86	0.55
n=1 total	11.80	6.09	5.14
n=2 vacuum	12.80	1.58	0.90
n=2 total	12.99	4.73	4.50
n=3 vacuum	19.74	2.61	1.53
n=3 total	20.41	3.80	2.93
n=4 vacuum	26.25	4.45	3.19
n=4 total	25.73	6.49	4.67

Table 1. $RMSE_{poly}$ for each scaled equilibrium set, for a linear, quadratic and cubic fit.

coeff	a	b	c	d	e	f	g	h	i
n=1 vacuum	0.13898	0.15842	-1.6741	-0.51686	-7.6899	18.737	-1.2555	65.15	-312.19
n=1 total	0.43305	-5.7	17.097	-2.7405	29.94	-99.267	-0.45866	49.966	-210.18
n=2 vacuum	0.14571	1.7142	-6.3854	-0.2497	-23.719	56.206	-3.1508	127.83	-327.38
n=2 total	0.14047	1.7732	-8.5336	-0.33719	-22.025	63.892	-3.1757	129.07	-286.34
n=3 vacuum	0.28269	1.6533	-6.7085	-0.33683	-34.041	76.084	-4.6137	180.18	-676.44
n=3 total	0.21942	1.8076	-7.1436	-0.56169	-28.501	67.55	-3.9637	171.31	-604.86
n=4 vacuum	0.36048	2.047	-8.1855	-0.50638	-42.161	91.007	-5.1487	219.78	-646.41
n=4 total	0.50969	0.78126	-6.1876	-1.1285	-35.518	85.061	-4.1725	208.44	-572.3

Table 2. All coefficients of 2D quadratic parametrisation of $\Delta\Phi_{opt}$, for all cases scanned using the scaled equilibrium set

3.3. Parametrisation of $\Delta\Phi_{opt}$

Figure 7 shows that for given n, $\Delta\Phi_{opt}$ is a smoothly varying function of (β_N, q_{95}). This allows the results to be parametrised with a simple analytic function, to allow researchers to estimate $\Delta\Phi_{opt}$, which will be useful for interpreting experimental data and for planning future experiments. The choice of a 2D polynomial function is motivated by ease of use and to provide sufficient degrees of freedom to fit the scan results in Figure 7 closely. Linear, quadratic and cubic 2D polynomials in (β_N, q_{95}) were fit to the data in Figure 7. To quantify the fit of each polynomial to the scaled equilibrium data, an RMSE between the polynomial and the scaled equilibrium set is used, defined below

$$RMSE_{poly} = \left(\sum_{i}^{N} (\Delta\Phi^{i}_{opt,set} - \Delta\Phi^{i}_{opt,poly})^2 / N \right)^{\frac{1}{2}} \tag{2}$$

where N here is the number of points in the scaled equilibrium set, $\Delta\Phi^{i}_{opt,set}$ are the optimum coil phases for each point in the scaled equilibrium set as computed by MARS-F, and $\Delta\Phi^{i}_{opt,poly}$ are the optimum coil phases predicted by the linear, quadratic or cubic 2D

polynomials. For each polynomial, the values of $RMSE_{poly}$ for all 8 datasets are listed in table 1. The table shows that while the quadratic fit is a significant improvement on the linear fit, the cubic fit is not significantly better at representing the data than the quadratic. Since this parametrisation is intended for use by researchers for planning experiments, the quadratic fit is used, as a compromise between accessibility and accuracy. Equation 3 describes the form of the 2D quadratic function, and table 2 lists the coefficient values of the 2D quadratic. In the following, let $\Delta\Phi_{opt,quad}$ be $\Delta\Phi_{opt}$ predicted by the 2D quadratic parametrisation, $x = \beta_N$ and $y = q_{95}$

$$\Delta\Phi_{opt,quad} = a(x^2y^2) + b(x^2y) + c(x^2) + d(xy^2) + e(xy) + f(x) + g(y^2) + h(y) + i \quad (3)$$

Across the bulk of the (β_N, q_{95}) domain the 2D quadratic is within 6 degrees of the computed scan in all datasets. However, when the plasma response is included, there are small horizontal 'stripes' in the (β_N, q_{95}) domain which correspond approximately to nq_a being immediately below an integer, where sharp peaks in the amplified kink-peeling response as computed by MARS-F are observed, as previously detected and explained in [22, 34]. These peaks cause a highly localised upward shift from the underlying trend of up to 20 degrees. These points do not significantly affect the 2D quadratic fit however, which is dominated by the bulk of the (β_N, q_{95}) domain outside the RFA peaks.

3.4. Uncertainty of the parametrisation

In order to quantify the uncertainty of the 2D quadratic compared to a full MARS-F computation as in [32, 35], a set of benchmarking points, consisting of 85 distinct time points from 31 distinct plasma discharges (49 time points from 17 $n = 1$ discharges, 36 timepoints from 14 $n = 2$ discharges), and their corresponding coil currents, equilibria and kinetic profiles, were collected from the ASDEX Upgrade experimental database. The equilibria, based on CLISTE [50] reconstructions which are routinely performed after each ASDEX Upgrade experiment, were read from the ASDEX Upgrade database. Using the AUGPED tool, analytic mtanh functions were fitted to experimental measurements aggregated over 20ms, of electron density n_e, electron temperature T_e, and ion temperature T_i, and a spline to toroidal bulk plasma rotation v_t, in order to produce the kinetic profiles for each benchmarking point. Figure 8 shows the data and fits of kinetic profiles for an example benchmarking point. Global plasma parameters (β_N, q_{95}) for each benchmarking point are summarised in figure 9. Plasma boundary shapes for the benchmarking equilibria and the reference equilibrium (30835 at 3.2s), are shown in figure 10. Each benchmarking point consists of a plasma equilibrium and plasma boundary reconstructed from magnetic measurements, kinetic profiles of n_e, T_e, T_i and v_t fitted to data from multiple diagnostics, and the experimentally applied RMP coil currents. For each benchmarking point, the vacuum field and plasma response was computed using the MARS-F code, to compute $b^{1,l}_{res}$ and $b^{1,u}_{res}$, and $\Delta\Phi_{opt}$ was then computed using Equation 1. Figure 11 shows the values of $\Delta\Phi_{opt}$ predicted by the 2D quadratic function,

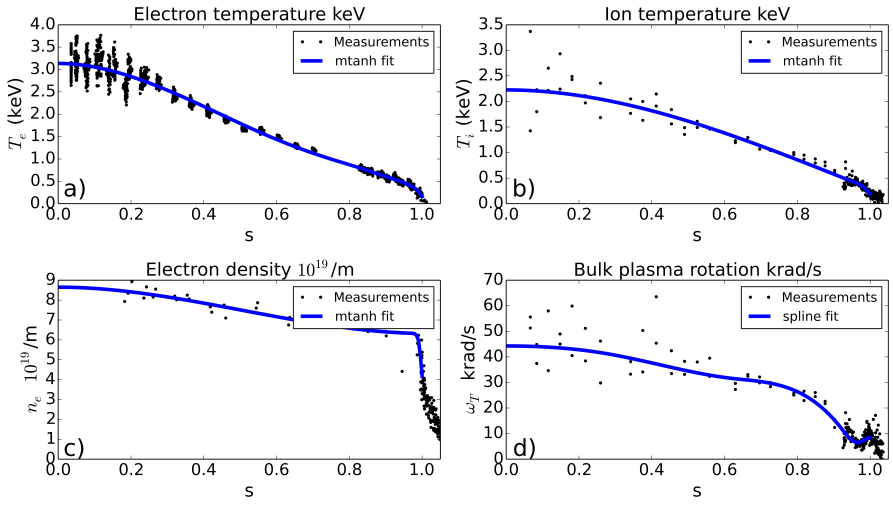

Figure 8. Kinetic data and fitted curves for ASDEX Upgrade discharge number 30641 at 4.0s, illustrating an example kinetic profile fit for a benchmarking point. The significant scatter in the spatially resolved experimental measurements is typical. a) mtanh function fitted to electron temperature data from the Thompson Scattering diagnostic [46] and Electron Cyclotron Emission diagnostic [47]. b) mtanh function fitted to ion temperature data from the Charge Exchange Recombination Spectroscopy diagnostic [48]. c) mtanh function fitted to electron density data, from the Thompson Scattering diagnostic, the Lithium Beam diagnostic [49] and interferometers. d) spline function fitted to toroidal bulk rotation data, from the Charge Exchange Recombination Spectroscopy diagnostics

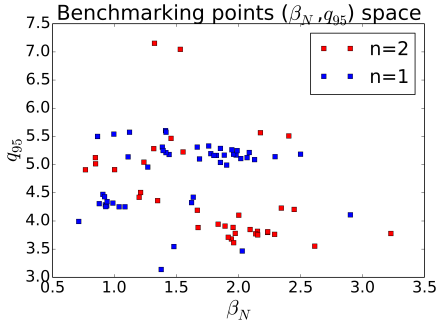

Figure 9. Experimental values of (β_N, q_{95}) used to benchmark the 2D quadratic parametrisation. Each point consists of a distinct equilibrium, plasma boundary, set of kinetic profiles and RMP coil currents.

compared with values computed using a MARS-F plasma response computation for the diverse set of benchmarking points, for both $n = 1$ and $n = 2$ RMP experiments. Performing this benchmarking for the $n = 3, 4$ scan is left for future work. To quantify the agreement between the 2D quadratic (Equation 3 with coefficients in Table 2) and the benchmarking points (computed with MARS-F for distinct equilibria and coil currents, and Equation 1), the RMSE between them is defined below, where N is now the number of benchmarking points

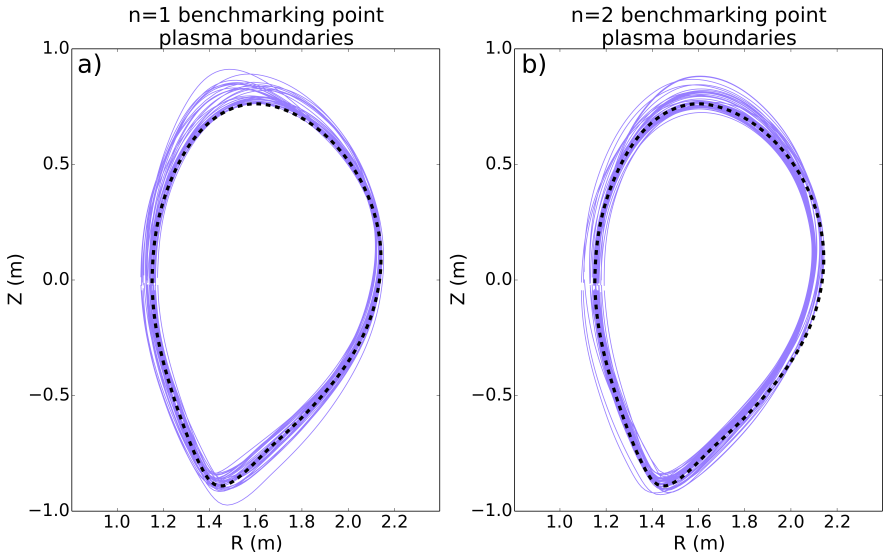

Figure 10. Plasma boundaries of each benchmarking point, and the boundary of the reference equilibrium (black dashed line). There is significant variation in boundary shape in the set of benchmarking points.

$$RMSE_{bench} = \left(\sum_{i}^{N} (\Delta\Phi^{i}_{opt,bench} - \Delta\Phi^{i}_{opt,quad})^2 / N \right)^{\frac{1}{2}} \tag{4}$$

The RMSE between the 2D quadratic function and the benchmarking points, is 7.8 for $n = 1$ vacuum predictions, 26.5 for $n = 1$ total predictions, 15.8 for $n = 2$ vacuum predictions, and 20.6 for $n = 2$ total predictions. Figure 11 shows the predictions of the 2D quadratic plotted against the MARS-F predictions. In Figure 2, it can be seen that the gradient of $|b^1_{res}|$ is low in the region of $\Delta\Phi_{opt}$, therefore misalignment on the order this deviation may be tolerated without a great effect on $|b^1_{res}|$. Therefore the agreement shown in Figure 11 is sufficient for experimental planning. As the figure shows, there are instances where the prediction of the 2D quadratic differs significantly from the MARS-F predictions for the benchmarking points. Several candidate causes for these deviations are now discussed.

3.5. Sources of uncertainty for $\Delta\Phi_{opt,quad}$

3.5.1. Rotation The benchmarking points have a widely varying rotation profiles, and core and edge rotation speeds. However, the rotation profile was held constant when the plasma response was computed for the (β_N, q_{95}) scan. In order to determine whether $\Delta\Phi_{opt}$ is sensitive to rotation, and therefore whether rotation may explain some of the scatter in Figure 11, $\Delta\Phi_{opt}$ was computed using the reference equilibrium, while the rotation profile was scaled from 0.1 to 10 times its experimental value. Figure 12 shows the computed values of $\Delta\Phi_{opt}$ as

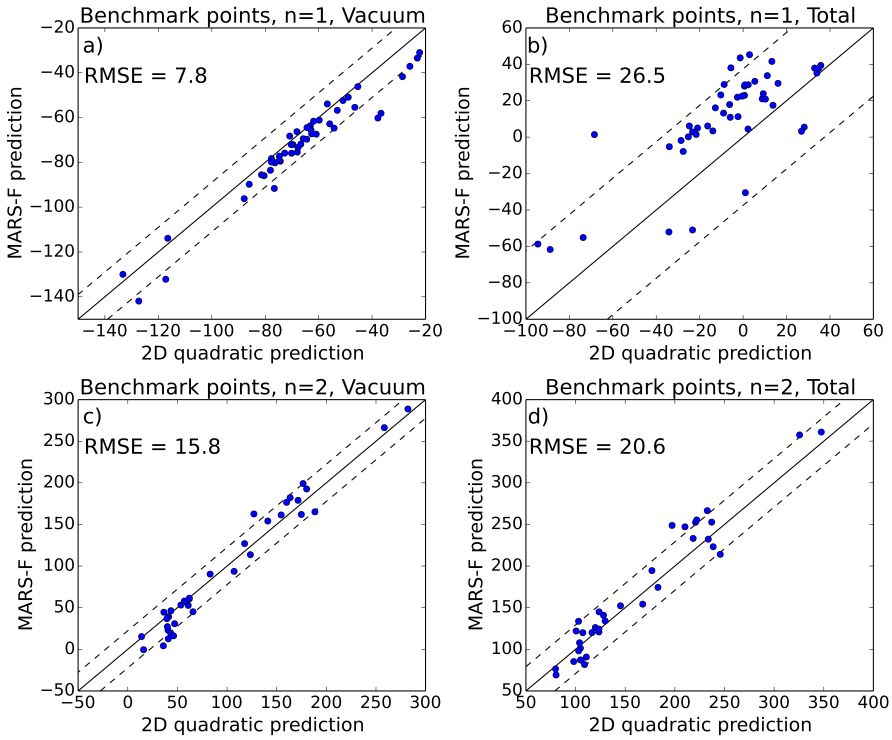

Figure 11. $\Delta\Phi_{opt}$ at each benchmarking point predicted by the 2D quadratic, with only β_N, q_{95} and n as input, plotted against $\Delta\Phi_{opt}$ at each benchmarking point predicted by a full MARS-F computation, with a plasma equilibrium, plasma boundary shape, coil currents and set of kinetic profiles as input. The 1:1 line is annotated on in solid black, and the dashed black lines are $RMSE_{bench}$ degrees from the 1:1. The MARS-F computation is the more rigorous approach, but the 2D quadratic is far simpler and quicker, and requires no specialist software or expertise.

rotation speed is changed. The plot shows that $\Delta\Phi_{opt}$ is insensitive to scaling of the rotation profile, to within 10 degrees.

3.5.2. Kinetic pedestal uncertainty As Figure 8 shows, the kinetic profiles required for the MARS-F computation are produced by fitting curves to experimental data. Any such fit has an associated uncertainty, and as the kinetic profiles are used as input to MARS-F it is possible that this uncertainty may propagate into the plasma response computations, or even the vacuum calculations by modifying the equilibrium near the edge. In this section, the effects of kinetic profile uncertainty on $\Delta\Phi_{opt}$ are investigated, by recomputing $\Delta\Phi_{opt}$ while changing the kinetic pedestal width within its uncertainty. Figure 13 shows the profiles used in the scan. The pedestal width is varied from -2σ to $+2\sigma$, where σ is the uncertainty in pedestal width derived from the original mtanh fit to the kinetic data. The equilibrium reconstruction was repeated for each pedestal width, such that the current and pressure profiles were consistent with the kinetic profiles. This resulted in slight changes to the pressure and q profiles, as shown in Figure 14 a), b) and c). The equilibrium reconstruction was

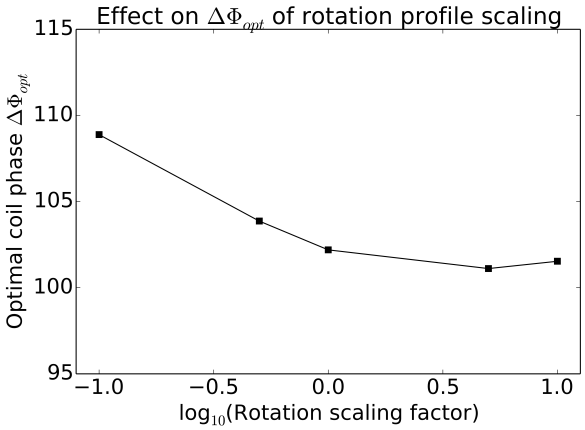

Figure 12. $\Delta\Phi_{opt}$ of the reference equilibrium computed by MARS-F, while the toroidal rotation profile is scaled by factors of 0.1 to 10. The result shows that $\Delta\Phi_{opt}$ is robust to rotation profile scaling.

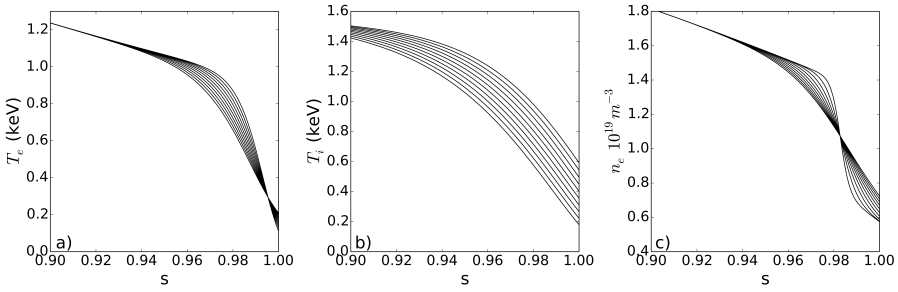

Figure 13. Profiles of the electron and ion temperature and the electron density are fitted to mtanh curves. The fit parameters, specifically the pedestal width, has an associated uncertainty σ. The profiles above represent a scan of the pedestal width from -2σ to 2σ.

performed using the CLISTE code [50], which computes the equilibrium based on magnetic measurements and kinetic profiles, and self-consistently includes the bootstrap current. For each set of self consistent kinetic profiles and equilibria, the optimal coil phase including the plasma response was computed using MARS-F. Figure 14 d) shows $\Delta\Phi_{opt}$ with varying pedestal width. The figure shows that $\Delta\Phi_{opt}$ is robust to uncertainties in the kinetic pedestal width, therefore it is unlikely to be the cause of the deviations in Figure 11.

3.5.3. Plasma Boundary As Figure 10 shows, the plasma boundaries of the benchmarking points vary widely, in particular many were significantly different to the reference equilibrium used to derive the 2D quadratic function. In a recent work [34], also using MARS-F and 30835 at 3.2s as reference equilibrium, $\Delta\Phi_{opt}$ was computed for a scan of the upper triangularity of the plasma boundary shape. It was shown that a change in the upper triangularity of the plasma boundary shape of 0.08, can result in a change to $\Delta\Phi_{opt}$ of 60 degrees. It seems likely then, that variations in the plasma shape may explain much of the scatter observed in Figure 11.

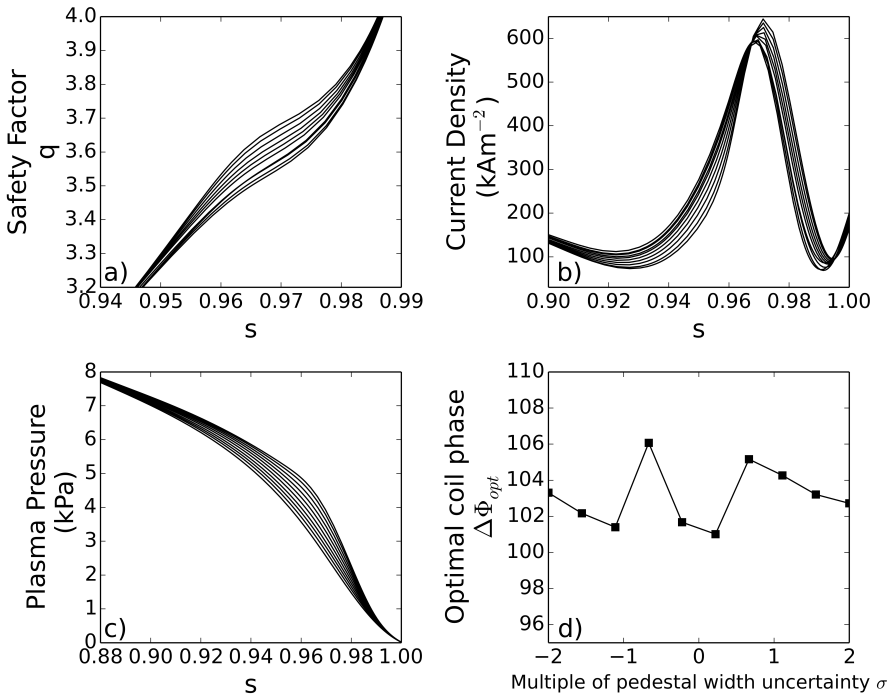

Figure 14. For each step in the kinetic profile uncertainty scan, the equilibrium was recomputed using CLISTE, causing changes to the equilibrium consistent with the kinetic profile changes. Figure a) shows the magnetic helicity, b) equilibrium current profile and c) the equilibrium current profile) . d) shows $\Delta\Phi_{opt}$ computed with MARS-F for each equilibrium in the kinetic profile scan. $\Delta\Phi_{opt}$ is also robust to pedestal width within $\pm 2\sigma$ of the fit uncertainty.

As well as a random error, Figure 10b) shows what appears to be a systematic deviation between the 2D quadratic and MARS-F predictions. The observation that the RMSE between the 2D quadratic and scan data is small, and also that the 2D quadratic is within 6 degrees of the scaled equilibrium data for the bulk of the domain (except the RFA peaks as previously described), indicates that this is not simply a fitting error. It may be that this deviation results from a systematic difference between the plasma boundaries of the $n = 1$ discharges, and the reference discharge used to derive the 2D quadratic. To answer this, a systematic study of the dependence of $\Delta\Phi_{opt}$ on the plasma boundary shape, and orientation and proximity to the RMP coils would be required, which is left for future work. Also in future works, the coefficients in table 2 may be recomputed using an equilibrium which has a boundary shape which is more representative of ASDEX Upgrade discharges, which may reduce the uncertainties.

4. Summary and Discussion

The effect of the plasma equilibrium parameters β_N and q_{95} on the optimal RMP coil phase $\Delta\Phi_{opt}$ is quantified for $n = 1 - 4$ RMP perturbations and ASDEX Upgrade plasmas. By scaling a standard ASDEX Upgrade reference equilibrium in plasma current and pressure, and computing the plasma response to an applied RMP field at each scaled point, the optimal coil phase $\Delta\Phi_{opt}$ as a function of (β_N, q_{95}) and n was computed. It was found that for given n and plasma shape, $\Delta\Phi_{opt}$ is a smoothly varying function of (β_N, q_{95}), allowing it to be parametrized with a simple 2D quadratic function. By computing $\Delta\Phi_{opt}$ using MARS-F for a large and diverse set of free boundary equilibria from distinct ASDEX Upgrade experiments, the accuracy of the 2D quadratic relative to MARS-F predictions was quantified. It was found that the 2D quadratic agrees with rigorous MARS-F computations (ie, for a given equilibrium, coil current set and experimental profiles) to within 7.8 degrees for $n = 1$ vacuum predictions, 26.5 degrees for $n = 1$ total predictions, 15.8 degrees for $n = 2$ vacuum predictions, and 20.6 degrees for $n = 2$ total predictions. The 2D quadratic is a sufficiently simple parametrization that $\Delta\Phi_{opt}$ can be computed rapidly for large datasets, and also that a coil phase optimisation feedback control system can be envisaged, which would change the coil phase to follow its optimal value throughout a plasma discharge. Benchmarking the 2D quadratic for $n = 3, 4$, quantifying thoroughly the effect of small misalignments on the mitigated ELM frequency, improving the accuracy of the 2D quadratic by use of a more representative reference equilibrium and by incorporating variation in the plasma boundary shape, and also refining this parametrization and tailoring it for other tokamaks, both existing and planned, is left for future work. Also left for future work is validating experimentally the optimal coil phase dependence on q_{95} and β_N, by measuring the ELM frequency during $\Delta\Phi$ scans at a range of q_{95} and β_N values.

Acknowledgements

This work has been carried out within the framework of the EUROfusion Consortium and has received funding from the Euratom research and training programme 2014-2018 under grant agreement No 633053, and is part-funded by the EPSRC through the Fusion Doctoral Training Network (grant number EP/K504178/1), and part-funded by the RCUK Energy Programme (under grant EP/I501045). To obtain further information on the data and models underlying this paper please contact PublicationsManager@ccfe.ac.uk. The views and opinions expressed herein do not necessarily reflect those of the European Commission.

References

[1] H. Zohm *et al*, 2015, *Nuclear Fusion*, **55**, 104010.
[2] H. Zohm, 1996, *Plasma Physics and Controlled Fusion*, **38**, 105–128.
[3] A. W. Leonard, 2014, *Physics of Plasmas*, **21**, 090501.
[4] A. Loarte *et al*, 2003, *Plasma Physics and Controlled Fusion*, **45**, 1549–1569.
[5] T. E. Evans *et al*, 2004, *Physical Review Letters*, **92**, 235003.
[6] Y. M. Jeon *et al*, 2012, *Physical Review Letters*, **109**, 035004.

[7] Y. Liang *et al*, 2007, *Physical Review Letters*, **98**, 265004.
[8] A. Kirk *et al*, 2013, *Nuclear Fusion*, **53**, 043007.
[9] W. Suttrop *et al*, 2011, *Physical Review Letters*, **106**, 225004.
[10] M. Bécoulet *et al*, 2009, *Nuclear Fusion*, **49**, 085011.
[11] M. F. Heyn *et al*, 2008, *Nuclear Fusion*, **48**, 024005.
[12] Y. Q. Liu *et al*, 2010, *Physics of Plasmas*, **17**, 072510.
[13] J. Park *et al*, 2007, *Physics of Plasmas*, **14**, 052110.
[14] J. Park *et al*, 2007, *Physical Review Letters*, **99**, 195003.
[15] M. J. Lanctot *et al*, 2013, *Nuclear Fusion*, **53**, 083019.
[16] C. Paz-Soldan *et al*, 2015, *Physical Review Letters*, **114**, 105001.
[17] A. D. Turnbull, 2012, *Nuclear Fusion*, **52**, 054016.
[18] Y. Q. Liu *et al*, 2000, *Physics of Plasmas*, **7**, 3681.
[19] M. J. Lanctot *et al*, 2010, *Physics of Plasmas*, **17**, 030701.
[20] M. J. Lanctot *et al*, 2011, *Physics of Plasmas*, **18**, 056121.
[21] J. D. King *et al*, 2015, *Physics of Plasmas*, **22**, 072501.
[22] S. R. Haskey *et al*, 2014, *Plasma Physics and Controlled Fusion*, **56**, 035005.
[23] A. Kirk *et al*, 2015, *Nuclear Fusion*, **55**, 043011.
[24] A. Kirk *et al*, 2013, *Plasma Physics and Controlled Fusion*, **55**, 015006.
[25] R. A. Moyer *et al*, 2012, *Nuclear Fusion*, **52**, 123019.
[26] I.T. Chapman *et al*, 2014, *Nuclear Fusion*, **54**, 083006.
[27] Y. Q. Liu *et al*, 2011, *Nuclear Fusion*, **51**, 083002.
[28] A. Kirk *et al*, 2011, *Plasma Physics and Controlled Fusion*, **53**, 065011.
[29] C. Paz-Soldan *et al*, 2016, *Nuclear Fusion*, **56**, 056001.
[30] A. H. Boozer, 2001, *Physical Review Letters*, **86**, 5059–5061.
[31] F. Orain *et al*, 2017, *Nuclear Fusion*, **57**, 022013.
[32] D. A. Ryan *et al*, 2015, *Plasma Physics and Controlled Fusion*, **57**, 095008.
[33] Y. Q. Liu *et al*, 2016, *Plasma Physics and Controlled Fusion*, **58**, 114005.
[34] L. Li *et al*, 2016, *Nuclear Fusion*, **56**, 126007.
[35] Y. Liu *et al*, 2016, *Nuclear Fusion*, **56**, 056015.
[36] A Wingen *et al*, 2015, *Plasma Physics and Controlled Fusion*, **57**, 104006.
[37] M. R. Wade *et al*, 2015, *Nuclear Fusion*, **55**, 023002.
[38] R. Nazikian *et al*, 2015, *Physical Review Letters*, **114**, 105002.
[39] T. E. Evans *et al*, 2008, *Nuclear Fusion*, **48**, 024002.
[40] T. E. Evans, 2013, *Journal of Nuclear Materials*, **438**, S11–S18.
[41] Y. Liang *et al*, 2010, *Physical Review Letters*, **105**, 065001.
[42] K. H. Burrell *et al*, 2005, *Plasma Physics and Controlled Fusion*, **47**, B37–B52.
[43] J. Park *et al*, 2008, *Nuclear Fusion*, **48**, 045006.
[44] M. E. Fenstermacher *et al*, 2008, *Physics of Plasmas*, **15**, 056122.
[45] H. Lütjens *et al*, 1996, *Computer Physics Communications*, **97**, 219–260.
[46] H. Murmann *et al*, 1992, *Review of Scientific Instruments*, **63**, 4941.
[47] W. Suttrop *et al*, 1996, *Practical Limitations to Plasma Edge Electron Temperature Measurements by Radiometry of Electron Cyclotron Emission*, (Technical Report IPP 1/306) Garching (DE): Max–Planck–Institut fr Plasmaphysik.
[48] E. Viezzer *et al*, 2012, *Review of Scientific Instruments*, **83**, 103501.
[49] M. Reich *et al*, 2004, *Plasma Physics and Controlled Fusion*, **46**, 797–808.
[50] P. J. McCarthy, 2011, *Plasma Physics and Controlled Fusion*, **54**, 015010.